Written by: Tim DeMonte

Lullyn Technologies

www.lullyn.com

Table of Contents

Disclaimer of Warranty

The technical descriptions, procedures, and computer programs in this document have been developed with the greatest of care and they have been useful to the author in a broad range of applications; however, they are provided as is, without warranty of any kind. Lullyn Technologies Inc. and the author of the document titled *Low Frequency Current Density Imaging Theory 1* make no warranties, expressed or implied, that the equations, programs, and procedures in this document or its associated software are free of error, or are consistent with any particular standard of merchantability, or will meet your requirements for any particular application. They should not be relied upon for solving a problem whose incorrect solution could result in injury to a person or loss of property. Any use of the programs or procedures in such a manner is at the user's own risk. The author and publisher disclaim all liability for direct, incidental, or consequent damages resulting from use of the programs or procedures in this document or the associated software.

Acknowledgements

I would like to express my appreciation to many people I have worked with over the past seven years on current density imaging projects. First, the people I regard as the pioneers of current density imaging: Greig Scott, Mike Joy and Mark Henkelman. The past and present graduate student members of the current density imaging research lab at the University of Toronto: Richard Yoon, Karshi Hasanov, Dinghui Wang, Angela Ma, John Paul Morgan, Charles Yan, Leili Torab, Maggie Kusano, Aaron Weinroth and others that I did not have the opportunity to meet. Collaborating scientists: Dawn Jorgenson, Adrian Nachman, Andrei Patriciu, Eung Je Woo, SukHoon Oh, and Jin Keun Seo. Technicians, engineers and undergraduate students: Franz Schuh, Cindy Wang, John Crowley, Sara Badiei, Jacques Philippe, Neil Wadehra, Rachel Chan, Jamin Sheriff, Roger Cheung, Mohammed Tariq Rafique, Rajat Gupta, Ruxandra Cioraca, Jessie Yen, Lev Vaisman, Basemah Fu, Randy Wang, Jim Hou, Jeremy Cruz, Jessica Liao, Rina Gupta, Liz Yang, Omair Naeem, Subhi Barakat, and Jack Lee. The many scientists from the imaging research group at Sunnybrook & Women's College Health Sciences Centre. My apologies for anyone I may have forgotten to include in this list.

Author's Comments

This document is a work in progress that contains a collection of some of my notes pertaining to current density imaging (CDI) theory. These notes were gathered from 1998 to 2005 based on my experience working in professor Mike Joy's CDI lab at the University of Toronto. The revision of February 2013 was merely to update the copyright notice and add these comments before making the document publicly available.

Tim DeMonte

1 Introduction

Low Frequency Current Density Imaging (LF-CDI) was developed by Greig C. Scott, Michael L.G. Joy and R. Mark Henkelman in 1988 at the University of Toronto in Canada [1, 2, 3 and 4]. LF-CDI is an imaging technique that measures electrical current density vectors in a volume of material/tissue which can be imaged using Magnetic Resonance Imaging (MRI). Measurements are performed by externally applying synchronous electrical current pulses to the material/tissue during an MRI acquisition. The magnetic fields produced by the applied current are encoded in the phase images of the MRI acquisition. The phase images are processed to compute the current density vectors. Performing CDI requires an MRI system, pulse synthesizer, current amplifier, low pass RF blocking filter, modified MRI pulse sequence and data processing software.

Externally applied current pulses have an amplitude of tens of mA and a duration of several ms to achieve a reasonable signal-to-noise ratio (SNR)[1]. The spatial resolution of LF-CDI is similar to MRI with a limit of about 1 mm^3 voxels for typical system receive coils (i.e. body and head coils) and higher resolution approaching 0.1 mm^3 voxels for smaller receive coils (e.g. 3" surface coil, custom designed receive coils). For the low frequency current pulses used in LF-CDI, the MRI system only measures the component of the magnetic field that is parallel to the main static field of the MRI system, B_0. To measure a complete current density vector field, measurement of all three orthogonal components of magnetic field is necessary; however, some recent work has demonstrated computation of a complete current density vector field with only one measured component of magnetic field [5, 6, 7 and 8]. The single component magnetic field methods are not covered in this document. Measurement of all three components of magnetic field requires orthogonal rotations of the object/subject. Further, as with most MRI techniques that use phase data, system phase errors are removed by phase differencing. The polarity of current pulses is cycled for each of the two phase difference datasets to ensure signal due to current is encoded. The scan time of an LF-CDI acquisition is typically 6 times higher than the corresponding MRI sequence (i.e. 3 orthogonal orientations x 2 phase cycles = 6) plus the time required to perform physical rotations of the object/subject.

Applications of LF-CDI include measurement of current density vectors in conductive solutions, conductive gels and biological tissues. The technique has been used to measure current density beneath surface electrodes [9, 10 and 11], current flow through gel-phantom models of biological systems [12], current flow in small animal models [10 and 13], measurement of chemical processes [14], and for enhancement of impedance imaging methods [6, 7, 8, 15, 16 and 17].

The theory of LF-CDI is described in full detail in [1, 2, 3 and 4]. The purpose of this document is to briefly review the theory and cover some topics such as nonlinear gradient distortion artifact in greater detail.

2 Fundamental Equations

LF-CDI uses MRI to measure components of magnetic field produced by externally applied current pulses. The curl of magnetic field is related to current density by Maxwell's equation [18]

$$\nabla \times \mathbf{H} = \mathbf{J} + \frac{\partial \mathbf{D}}{\partial t} \tag{1}$$

[1] Assuming the electrical current pulse has rectangular shape, the CDI signal strength, i.e. slope of phase ramp, is directly proportional to the amplitude of the current pulse and the CDI noise, referred to as σ_J in Section 7, is inversely proportional to the duration of the current pulse. Therefore, the CDI SNR is directly proportional to the product of current amplitude and current duration which is the total charge of the current pulse (expressed in units of Coulombs). Experimentally, approximately 100 μC is the lower limit of reasonable CDI SNR for 3.8 mm^3 voxels and typical MRI SNR in tissue (assuming a typical Fast 3D GRE sequence).

where **H** is the magnetic field intensity in A/m, **J** is the conduction current density in A/m^2 and the time-varying electric flux density, $\partial \mathbf{D} / \partial t$, represents displacement current density in A/m^2. LF-CDI uses rectangular DC current pulses that produce only conduction current. Therefore, only the quasi-static version of Maxwell's equation (i.e. the differential form of Ampere's Law) is required to relate current density to magnetic field

$$\mathbf{J} = \nabla \times \mathbf{H} \qquad (2)$$

For media with low magnetic susceptibility, i.e. $\chi_m < 10^{-5}$, permeability, μ, can be considered approximately equal to μ_0 ($\mu_0 = 4\pi \times 10^{-7}$ H/m). The expansion of equation (2) in Cartesian coordinates is given by

$$\mathbf{J} = \frac{1}{\mu_0}\left[\left(\frac{\partial B_z}{\partial y} - \frac{\partial B_y}{\partial z}\right)\mathbf{a}_x + \left(\frac{\partial B_x}{\partial z} - \frac{\partial B_z}{\partial x}\right)\mathbf{a}_y + \left(\frac{\partial B_y}{\partial x} - \frac{\partial B_x}{\partial y}\right)\mathbf{a}_z\right] \qquad (3)$$

where B_x, B_y and B_z are orthogonal magnetic field components in units of Tesla (T) and $\mathbf{a}_x$, $\mathbf{a}_y$ and $\mathbf{a}_z$ are orthogonal unit vectors in the Cartesian coordinate system. The angle, Γ, encoded in the phase data of an MRI acquisition is related to the component of magnetic field, B_J, produced by the externally applied current by [1]

$$\Gamma = \gamma B_J T_c \qquad (4)$$

where γ is the gyromagnetic ratio ($\gamma = 2\pi 42.58 \times 10^6$ radians/Ts for a 1.5 T MRI system) and T_c is the duration of the applied current pulse. B_J is the component of the magnetic field that is parallel to the static field B_0. Phase data is acquired for three orthogonal orientations of the object/subject to obtain the components B_x, B_y and B_z using equation (4). Current density vectors are computed from the partial spatial derivatives of B_x, B_y and B_z using equation (3).

3 MRI Sequences

Most MRI sequences can be modified to perform LF-CDI provided they meet the following specifications:

- There are several milliseconds between the initial excitation pulse and the readout gradient where no RF or gradient pulses exist. This is the time interval in the sequence when a current pulse(s) could potentially be applied without disrupting the MRI acquisition[2].
- The entire dataset is acquired twice to allow for implementation of phase cycling. Current pulses of reverse polarity should be applied on each subsequent phase cycle to maximize CDI signal; however, it is also okay to apply current on one phase cycle and no current on the subsequent phase cycle. It is preferable to acquire two lines of k-space corresponding to two phase cycles consecutively to minimize some motion artifacts.
- Current pulses affect magnetization in a similar manner as gradient pulses. Any sequence that specifies balanced gradient pulses (e.g. steady state free precession (SSFP)) must also have balanced current pulses.

Examples of an LF-CDI sequence based on a spin echo sequence and a fast gradient recalled sequence are shown in figures 1(a) and 1(b), respectively. The reverse polarity phase cycle is shown as a dotted line for the fast gradient recalled echo sequence in figure 1(b).

[2] Applying too much current at any time during the sequence will cause greater than π phase shift over a distance of one voxel resulting severe loss of MR signal [3].

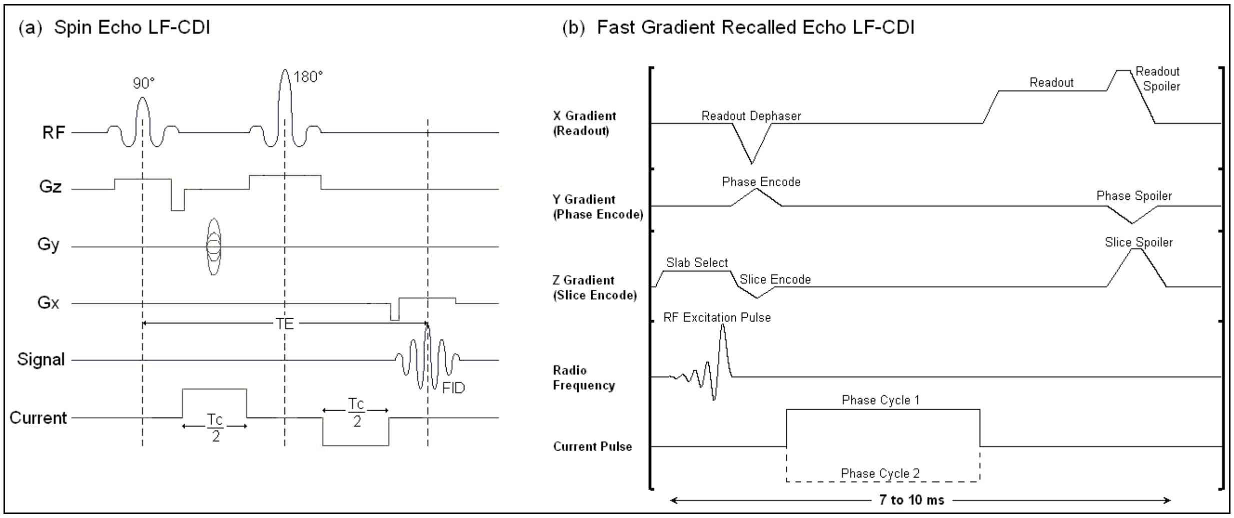

Fig. 1: Examples of implementations of LF-CDI sequences for (a) spin echo; and for (b) fast gradient recalled echo.

4 Noise Masking

Noise in phase data is masked out by using the magnitude data to create a binary mask. The threshold for creating the binary mask can be determined from

$$threshold = \frac{2}{\sqrt{\pi}} \cdot \mu \cdot (factor) \quad (5)$$

where μ is the mean value of a group of voxels taken from a zero-signal region of the magnitude data and *factor* is an arbitrarily selected quality factor. The factor $2/\sqrt{\pi} \cdot \mu$ is an estimate of the standard deviation (i.e. noise) of the magnitude data [19].

Noise masks are generated for each of the B_x, B_y and B_z datasets. Subsequent processing steps that apply the masks to phase data should use a mask that is a combination of all three masks (i.e. multiplication of all three binary masks with each other) to ensure that all six of the spatial derivatives shown in equation (3) have a value of zero at points where current density cannot be computed due to low MR signal.

5 Phase Unwrapping

Phase data from an MRI acquisition is in general wrapped between -π and π radians. Unwrapping phase along one line through phase data is relatively straightforward and robust to noise. The steps for one dimensional (1D) phase unwrapping are given in this section. Extending this method to two dimensions (2D) is not straightforward. So-called 'residues' are formed in a plane of noisy wrapped phase data [20] and these residues can cause virtually any phase unwrapping algorithm to fail. 2D phase unwrapping algorithms generally start by identifying residues and subsequently working around them. Many 2D phase unwrapping algorithms can be extended to three dimensions (3D) in a straightforward manner.

Current density processing can be accomplished using only 1D phase unwrapping provided that the unwrapping is performed along the same direction that a spatial derivative is taken and that the spatial derivative is estimated by convolution with an appropriate template (see next section). 3D phase unwrapping is required if the magnetic vector field is desired. Slice-to-slice phase offsets must also be removed if 3D phase unwrapping is performed on 2D multi-slice MRI datasets. Slice-to-slice phase offsets can be avoided by using 3D MRI sequences where the slice direction is Fourier encoded.

Let us define a wrapping operator, W, such that [20]

$$\psi(n) = W\{\varphi(n)\} \tag{6}$$

where $\psi(n)$ is the wrapped phase data and $\varphi(n)$ is the unwrapped phase data. Using Itoh's method of one dimensional phase unwrapping [21], the unwrapped phase is obtained by the summation of the wrapped differences of the wrapped phase data

$$\varphi(m) = \varphi(0) + \sum_{n=0}^{m-1} W\{\Delta\{W\{\varphi(n)\}\}\} \tag{7}$$

The steps for performing Itoh's are listed here [20]:

1. Compute phase differences $D(i) = \psi(i+1) - \psi(i)$ for i = 0,…,N-2.
2. Compute wrapped phase differences $\Delta(i) = \arctan\{\sin D(i), \cos(D(i)\}$ for i = 0,…,N-2.
3. Initialize first unwrapped value $\varphi(0) = \psi(0)$.
4. Unwrap by summing the wrapped phase differences $\varphi(i) = \varphi(i-1) + \Delta(i-1)$ for i = 1,…,N-1.

2D phase unwrapping algorithms are discussed in detail in [20]. Some of the algorithms in [20] can be extended to 3D in a straightforward manner. An example of an implementation of 3D phase unwrapping is given in [22].

6 Spatial Derivatives

Numerical differentiation can be performed by convolution of unwrapped phase difference data with Sobel operators [1, 2, 3, 4 and 23]. Using this method, the spatial derivatives of the J_z component of equation (3) can be estimated as

$$\frac{\partial B_y}{\partial x} \approx \frac{1}{\mu_0}\left(\frac{1}{8\cdot\Delta x}\begin{bmatrix}-1 & 0 & 1\\ -2 & 0 & 2\\ -1 & 0 & 1\end{bmatrix} * \left[\frac{\varphi_y}{\gamma T_c}\right]\right) \tag{8}$$

$$\frac{\partial B_x}{\partial y} \approx \frac{1}{\mu_0}\left(\frac{1}{8\cdot\Delta y}\begin{bmatrix}1 & 2 & 1\\ 0 & 0 & 0\\ -1 & -2 & -1\end{bmatrix} * \left[\frac{\varphi_x}{\gamma T_c}\right]\right) \tag{9}$$

where φ_y and φ_x are the unwrapped phase difference datasets corresponding to measurements of B_y and B_x, respectively. One dimensional phase unwrapping is sufficient when Sobel operators are used for estimating derivatives. Unwrapping must be performed in the same direction as the spatial derivative is taken (e.g. unwrapping is performed along x for equation (8)). Other derivative templates may be used. Three dimensional templates [2] such as

$$\frac{1}{32\Delta x}\left[\begin{Bmatrix}1 & 2 & 1\\ 2 & 4 & 2\\ 1 & 2 & 1\end{Bmatrix};\begin{Bmatrix}0 & 0 & 0\\ 0 & 0 & 0\\ 0 & 0 & 0\end{Bmatrix};\begin{Bmatrix}-1 & -2 & -1\\ -2 & -4 & -2\\ -1 & -2 & -1\end{Bmatrix}\right] \tag{10}$$

where the brace brackets {} indicate the layers of the 3D matrix, have the advantage of being symmetric in the plane orthogonal to the direction a spatial derivative is being taken. These larger templates, however, cause more filtering and data smoothing than may be desired.

Smaller templates may also be used [3 and 10] with the possible advantage being able to compute current density values along edge voxels near the boundary between conductive and nonconductive media [10]. Three examples of such edge voxel computations are shown in figure 2 for the voxels labeled 'a', 'b' and 'c'. For voxel 'a', 1x2 and 2x1 templates are combined, as indicated with shaded gray voxels, to estimate the derivative. For voxel 'b', 1x3 and 2x1 templates are combined to estimate the derivative and for voxel 'c', 1x3 and 3x1 templates are used to estimate the derivative. Examples of 1x2 and 1x3 templates are given in equations (11) and (12), respectively. The estimates of these derivatives near edges can be very noisy due to the small template size and often lower quality of the data. Further, templates with only two voxels have an inherent geometric offset whereby the computed derivative lies halfway between the two voxels. Such an offset could be corrected using interpolation/extrapolation techniques. Other template sizes and shapes are possible such as a 3x3x3 template that adapts to conductivity boundaries by setting values located in the nonconductive media to zero and adjusting all other values to make an optimal estimate of the derivative.

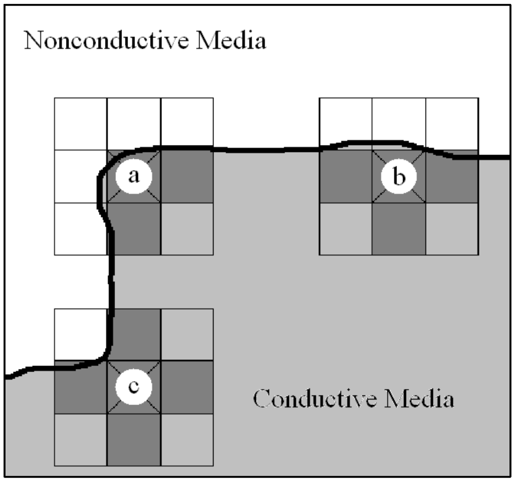

Fig. 2: Derivative templates used to estimate derivatives for voxels located near boundary between conductive and nonconductive media.

A 1x2 template has the form

$$\frac{1}{\Delta x}\begin{bmatrix}-1 & 1\end{bmatrix} \tag{11}$$

and a 1x3 template has the form

$$\frac{1}{2\cdot\Delta x}\begin{bmatrix}-1 & 0 & 1\end{bmatrix}. \tag{12}$$

Another variation would be to compute current densities at points that are either 8-connected (i.e. an interior point) or points that are 4-connected (e.g. point 'c' in figure 2). This method would compute fewer points than the above method. However, this method has the advantage of being able to make use of efficient 4-connected and 8-connected erosion/dilation image processing algorithms for fast processing. Such a method could be extended to 3D in a straightforward manner.

If the goal of a particular CDI experiment is to compute total current into or out of a volume, it may be desirable to use the 1x2 template given in equation (11) for computing derivatives throughout the dataset. The reason for this is that the numerical method used for computing the surface integral over the volume of interest will require a more localized estimation of the current density vector field to ensure that divergence of the current density vector field tends towards zero as expected ($\nabla\cdot\mathbf{J}=0$ if there are no measurable current sources in the media).

7 Noise Analysis

A full derivation of noise analysis for LF-CDI is given in [3 and 4]. The main result gives the standard deviation, i.e. the "noise" in CDI SNR, for a single voxel of data in an LF-CDI acquisition:

$$\sigma_J = \frac{1}{2\gamma\mu_0 T_c SNR}\sqrt{\left(\frac{F_x}{\Delta x}\right)^2+\left(\frac{F_y}{\Delta y}\right)^2} \tag{13}$$

where Δx and Δy are voxel dimensions and F_x and F_y are corresponding noise weights that are tabulated in [3] for several derivative templates. For example, F_x and F_y have a value of $\frac{\sqrt{3}}{4}$ for the templates given in equations (8) and (9); and F_x has a value of $\frac{1}{\sqrt{2}}$ for the templates given in equations (11) and (12). The *SNR* in equation (13) is the signal-to-noise ratio (SNR) of the MRI acquisition. From equation (13), noise can be reduced in an LF-CDI acquisition by increasing the duration of the current pulse, T_c, increasing the SNR of the MRI acquisition (i.e. use a more appropriate receive coil), using a larger voxel size and using a derivative template with more non-zero terms. Using a larger derivative template has the undesirable effect of averaging more magnetic field data resulting in a less localized computation of **J**.

8 Artifacts

The major artifacts associated with LF-CDI are listed in Table 1. Table 1 also includes suggestions for reducing each type of artifact.

Table 1: Artifacts in LF-CDI

Description of Artifact	Suggested Method of Reducing Artifact
Misalignment of B_x, B_y and B_z datasets due to nonlinear gradient field distortion of MRI system	• Measure nonlinear gradient distortion and correct for it
High phase gradients due to high current pulse amplitude	• Reduce current pulse amplitude to achieve good signal in regions of interest
Magnetic susceptibility of objects in experiment	• Replace high susceptibility materials with lower ones where possible (e.g. electrode materials) • Use acquisition/processing susceptibility reduction methods such as [24 and 25]
MR signal loss due to RF shielding	• Use smaller electrodes, less electrodes, electrodes with lower conductivity or cut electrodes in a way that reduces large surface areas
Processing/numerical artifacts	• Use different processing approach such as different derivative template size

The first artifact listed in Table 1, misalignment due to gradient field distortion, will be explained in further detail below since it causes the most problems in LF-CDI and removing this artifact is relatively difficult. For LF-CDI, the three datasets corresponding to the three orthogonal orientations of the object/subject must be registered (i.e. aligned) with each other before combining the data to compute current density vectors. This registration is not possible for large objects/subjects (i.e. >10 cm) whose datasets are geometrically distorted by nonlinearities in the MRI system gradient fields. In general, the nonlinearities associated with the three gradient fields, G_x, G_y and G_z, are different from each other and are not spherically symmetric about the magnetic center.

To demonstrate nonlinear gradient distortion, let **r** represent a set of position vectors in lab space with a spatial sampling rate corresponding to the sampling rate of the acquired datasets. Let $\mathbf{r}^g$ represent a set of position vectors in "gradient" space that have undergone a transformation due to the nonlinearities of the system gradient fields. The conceptual steps for obtaining a correction dataset and applying it to an arbitrary MRI dataset are listed below:

Steps to Obtain a Correction Dataset:

1. Specify the geometry of a standard phantom (e.g. 3D array of spherical objects having 8 mm diameter spheres with 15 mm center-to-center spacing).
2. Create an ordered set of position vectors, **rs** space, where each vector points to the location of the center of each sphere (figure 3(a)).
3. Acquire an MRI dataset of the standard phantom that shows the positions of spheres.

4. Apply edge enhancement filtering to the data to sharpen the edges of spheres.
5. Create an ordered set of sphere location vectors by applying a "sphere search" algorithm to find spheres at estimated locations and use center of mass (COM) computation to locate centers of spheres. Assume voxel sizes according to **r** space and the result will be a measurement of $\mathbf{r}^g$ sphere locations in **r** space distances. It is highly recommended to use adaptive algorithms for both "sphere search" and COM bounding box sizing that bases the next guess on the previous result(s) to accommodate severe distortions towards the edges of the field of view (FOV). Further, it is recommended that the algorithms are robust to cases of missing spheres. An example of a COM bounding box is shown as a cube surrounding a sphere for $\mathbf{rs}^g$ position vector in figure 3(a).
6. Regrid the **rs** space (figure 3(a)) sphere position vectors to the **r** space (figure 3(b)) positions of the MRI acquisition (e.g. 480 mm FOV / 256 samples = 1.875 mm voxel spacing) using an interpolation technique such as 3D cubic spline.
7. Save the dataset containing ordered $\mathbf{r}^g$ position vectors with index spacing corresponding to the MRI acquisition's voxel spacing (i.e. **r** space) as the "correction" dataset.

Steps to Apply Correction to an Arbitrary MRI Dataset:

1. At position ijk in the arbitrary MRI dataset, lookup the corresponding position vector in the ordered $\mathbf{r}^g$ position vector dataset. The difference between the **r** space and $\mathbf{r}^g$ space position vectors at point ijk indicates the required translation at point ijk.
2. Use interpolation to obtain a data value at the point $\mathbf{r}^g_{ijk}$ in the arbitrary MRI dataset.
3. Translate this point to $\mathbf{r}_{ijk}$ in the arbitrary MRI dataset.
4. Compute all necessary spatial derivatives of the $\mathbf{r}^g$ space position vectors as indicated in equation (14). The determinant of the matrix in equation (14) is the Jacobian of the transformation. The Jacobian is required to correct the signal intensity of the translated data. Figure 3(b) shows that, in general, the size and shape of the voxels in **r** space and $\mathbf{r}^g$ space are different and have different volumes. The data from the arbitrary MRI dataset has a signal intensity that corresponds to $\mathbf{r}^g$ space. Each translated data point at ijk must be multiplied by its corresponding Jacobian to correct for signal intensity.

The Jacobian of the $\mathbf{r}^g$ space position vector dataset is given by

$$J_{ijk} = \det\begin{bmatrix} \frac{\partial r_x^g}{\partial x} & \frac{\partial r_y^g}{\partial x} & \frac{\partial r_z^g}{\partial x} \\ \frac{\partial r_x^g}{\partial y} & \frac{\partial r_y^g}{\partial y} & \frac{\partial r_z^g}{\partial y} \\ \frac{\partial r_x^g}{\partial z} & \frac{\partial r_y^g}{\partial z} & \frac{\partial r_z^g}{\partial z} \end{bmatrix} \tag{14}$$

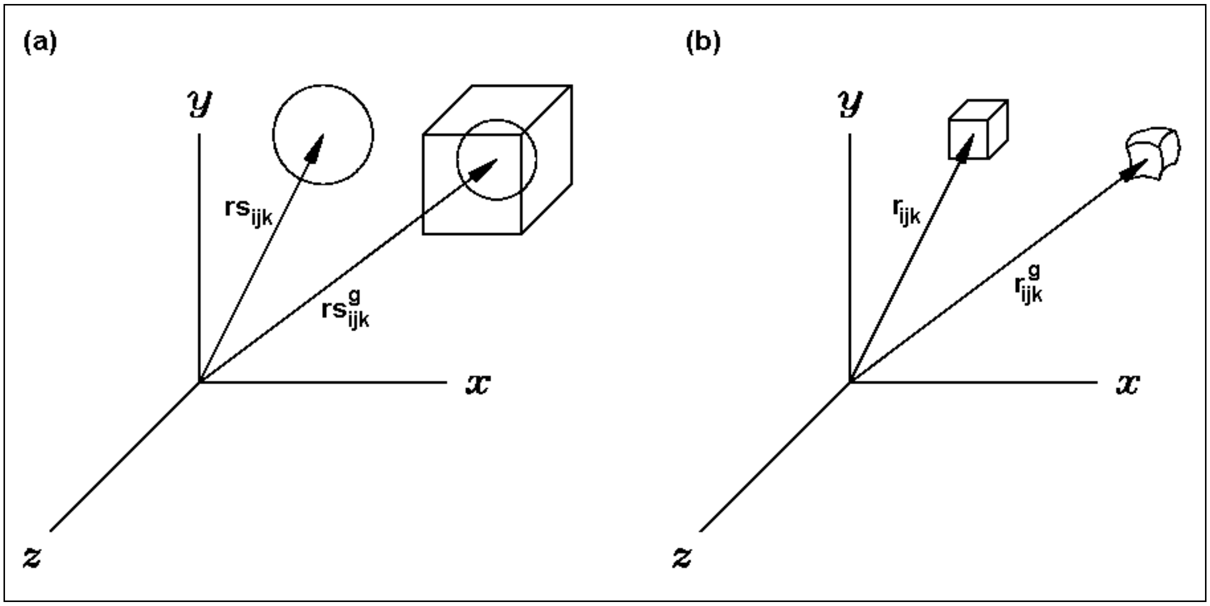

Fig. 3: (a) **rs** space is an ordered set of position vectors where each vector points to the center of a sphere in lab space. $\mathbf{rs}^g$ space is the corresponding ordered set of position vectors where each vector points to the center of a sphere in gradient space. A cube is shown surrounding an $\mathbf{rs}^g$ sphere to indicate a typical bounding box used for the center of mass (COM) computation. (b) **r** space is an ordered set of position vectors specifying voxels in lab space. $\mathbf{r}^g$ space is the corresponding set of position vectors specifying voxels in gradient space. $\mathbf{r}^g$ space is a regridded (i.e. interpolated) version of $\mathbf{rs}^g$ space with spatial resolution corresponding to the spatial resolution of an arbitrary MRI dataset that is to be corrected. In general, the size, shape and volume of the voxels in **r** space differ from those in $\mathbf{r}^g$ space as indicated by the voxels shown in (b).

Distortion correction of an arbitrary MRI dataset as described above applies only to MR magnitude data. This correction is useful for LF-CDI because the magnitude datasets are used to guide the process of data alignment between the three datasets corresponding to B_x, B_y and B_z measurements. However, further steps are required to correct the phase datasets that are used to compute current density vectors. One approach to this correction is to apply the distortion correction steps to the phase datasets. For this approach, there are two important modifications of the above listed correction steps: (1) the phase datasets must first be unwrapped in three dimensions[3], and (2) multiplication by the Jacobian to correct signal intensity is not required for phase data. Another approach to correcting distortion in the current density vectors is to process the phase data without correction to obtain the six spatial derivatives shown in equation (3). The spatial derivatives can then be corrected according the steps above. This approach avoids the necessity of a 3D phase unwrapping process (i.e. 1D phase unwrapping is sufficient); however, the derivatives are taken with respect to $\mathbf{r}^g$ space and require further correction to give derivatives with respect to **r** space. It turns out that this correction is accomplished once again by multiplication by the Jacobian of the $\mathbf{r}^g$ space position vector dataset. In this case, however, it is the spatial coordinate system that the derivatives are taken with respect to that is corrected rather than the signal intensity.

9 References

[1] Greig Cameron Scott. Current Density Imaging by Magnetic Resonance. MASc thesis, University of Toronto, 1989.

[3] If the MRI acquisition is a 2D multi-slice type, slice-to-slice phase offsets must first be removed before applying a 3D phase unwrapping process. For 3D slab acquisitions this step is not necessary.

[2] G. C. Scott, M. L. G. Joy, R. L. Armstrong, and R. M. Henkelman. Measurement of nonuniform current density by magnetic resonance. *IEEE Transactions on Medical Imaging*, Vol. 10, No. 3, pp. 362-374, 1991.

[3] G. C. Scott, M. L. G. Joy, R. L. Armstrong, and R. M. Henkelman. Sensitivity of Magnetic Resonance Current Density Imaging. *J. Mag. Res*., 97, pp. 235-254, 1992.

[4] Greig Cameron Scott. *NMR Imaging of Current Density and Magnetic Fields*. PhD thesis, University of Toronto, 1993.

[5] J.K.Seo, O. Kwon, B.I. Lee and E.J. Woo. Reconstruction of current density distributions in axially symmetric cylindrical sections using one component of magnetic flux density: computer simulation study. *Physiol Meas.*, Vol. 24, No. 2, pp. 565-577, May 2003.

[6] J.K. Seo, J.R. Yoon, E.J. Woo, O. Kwon. Reconstruction of conductivity and current density images using only one component of magnetic field measurements. *IEEE Trans Biomed Eng.*, Vol. 50, No. 9, pp. 1121-4, September 2003.

[7] Ozlem Birgul, B Murat Eyuboglu, and Y Ziya Ider. Experimental Results for 2D Magnetic Resonance Electrical Impedance Tomography (MR-EIT) using Magnetic Flux Density in One Direction, *Physics in Medicine and Biology*, Vol. 48, pp. 3485-3504, 2003.

[8] Y Ziya Ider and Serkan Onart. Algebraic Reconstruction for 3D Magnetic Resonance Electrical Impedance Tomography (MREIT) Using One Component of Magnetic Flux Density, *Physiological Measurement*, Vol. 25, pp 281-294, 2004.

[9] T.P. DeMonte, A. Patriciu, M.L.G. Joy and J.J. Struijk. Current Densities Produced by Surface Electrodes: Comparison of MRI measurements and Finite Element Modeling. *ISMRM* Conference Abstract, 2001.

[10] Tim DeMonte. *Multi-slice Current Density Imaging: Implementation and Applications*. MASc thesis, University of Toronto, 2001.

[11] T.P. DeMonte, P.D. Gadsby, P.F. Meyer and M.L. Joy. Measurement of Edge Effects in Automatic External Defibrillation Electrodes using Current Density Imaging. *ISMRM* Conference Abstract, 2005.

[12] R.S. Yoon, T.P. DeMonte, L. Organ and M.L.G. Joy. Study of current distribution for a non-invasive breast cancer detection device. *IEEE EMBS* Conference Abstract, 2003.

[13] Richard S. Yoon, Tim P. DeMonte, Karshi F. Hasanov, Dawn B. Jorgenson, and Michael L.G. Joy. Measurement of Thoracic Current Flow in Pigs for the Study of Defibrillation and Cardioversion. *IEEE Transactions on Biomedical Engineering*, Vol. 50, No. 10, October 2003.

[14] Katrina Beravs, Alojz Demsar, and Franci Demsar. Magnetic Resonance Current Density Imaging of Chemical Processes and Reactions. *J. Mag. Res.*, 137, pp. 253-257, 1999.

[15] S.H. Oh, J.Y. Han, S.Y. Lee, M.H. Cho, B.I. Lee, E.J. Woo. Electrical conductivity imaging by magnetic resonance electrical impedance tomography (MREIT). *Magn Reson Med.*, Vol. 50, No. 4, pp. 875-8, October 2003.

[16] O. Birgul, B.M. Eyuboglu, and Y.Z. Ider. Current constraint voltage scaled reconstruction (CCVSR) algorithm for MR-EIT and its application with different probing current patterns, Physics in Medicine and Biology, Vol.48, No.5, pp.653-671, 2003.

[17] Karshi F. Hasanov, Angela W. Ma, Richard S. Yoon, Adrian I. Nachman and Michael L.G. Joy. A New Approach to Current Density Impedance Imaging. *IEEE EMBS* Conference Abstract, 2004.

[18] William H. Hayt, Jr. *Engineering Electromagnetics Fifth Edition*, New York, NY: McGraw-Hill, Inc., 1989.

[19] M.L. Joy. The measurement of Signal and Noise from a Magnitude Magnetic Resonance Image and the estimation of phase noise. *Unpublished Lecture Notes*, 1999.

[20] Dennis C. Ghiglia and Mark D. Pritt. *Two-Dimensional Phase Unwrapping: Theory, Algorithms and Software*, New York, NY: John Wiley & Sons, Inc., 1998.

[21] K. Itoh. Analysis of phase unwrapping problem. *Applied Optics*, Vol. 21, No. 14, pp 2470, July 15, 1982.

[22] R. Cusack and N. Papadakis. New Robust 3-D Phase Unwrapping Algorithms: Application to Magnetic Field Mapping and Undistorting Echoplanar Images, *NeuroImage*, **16**, pp. 754-764, 2002.

[23] I. Sobel. An isotropic 3 x 3 image gradient operator. In H. Freeman, editor, *Machine Vision for Three-Dimensional Scenes*, pages 376-379. Academic Press, 1990.

[24] H. Chang and M. Fitzpatrick. A Technique for Accurate Magnetic Resonance Imaging in the Presence of Field Inhomogeneities, *IEEE Trans. On Medical Imaging*, Vol. 11, No. 3, pp. 319-329, September 1992.

[25] Jacques Philippe. Develop algorithms for removing the spatial image distortions caused by imperfections in the MR imager. University of Toronto Ungraduate Thesis, 2004.